

## Supporting Information

### **Sustainable lithium-ion batteries based on Metal-free tannery waste biochar**

Pejman Salimi,<sup>a,b</sup> Sebastiano Tieuli,<sup>c</sup> Somayeh Taghavi,<sup>c</sup> Eleonora Venezia,<sup>a,b</sup> Silvio Fugattini,<sup>a</sup> Simone Lauciello,<sup>a</sup> Mirko Prato,<sup>a</sup> Sergio Marras,<sup>a</sup> Tao Li,<sup>d</sup> Michela Signoretto,<sup>c</sup> Paola Costamagna,<sup>b</sup> Remo Proietti Zaccaria<sup>\*a,e</sup>

<sup>a</sup> *Istituto Italiano di Tecnologia, via Morego 30, Genova 16163, Italy*

<sup>b</sup> *Department of Chemistry and Industrial Chemistry, University of Genova, via Dodecaneso 31, I-16146 Genova, Italy*

<sup>c</sup> *CATMAT Lab, Department of Molecular Sciences and Nanosystems, Ca' Foscari University Venice and INSTM Consortium, RU of Venice, Via Torino 155, 30172 Venezia Mestre, Italy*

<sup>d</sup> *Key Laboratory of Liquid-Solid Structural Evolution and Processing of Materials of Ministry of Education, State Key Laboratory of Crystal Materials, Shandong University, Jinan, 250061, PR China*

<sup>e</sup> *Ningbo Institute of Materials Technology and Engineering, Chinese Academy of Sciences, Ningbo 315201, China*

\* Corresponding author. E-mail: Remo.Proietti@iit.it

## The pyrolysis process to synthesize of Tannery Waste Activated Carbons biochar

The pyrolysis process was carried out by a laboratory-scale prototype plant (Carbolite custom model EVT 12/450B). The experimental equipment consists of a vertical tubular furnace split into two halves along its length. The pyrolysis was performed in a fixed bed quartz tube equipped with a porous septum to hold the sample and to let the gas pass through, at the same time. The end flange of the quartz tube was connected to the quenching system through a heated outlet pipe (ca. 200°C) to prevent condensate build-up. The quenching system consisted of a first condenser, water-cooled at 20°C, which was linked to a series of glass condensers, cooled at 0°C in an ice bath, for collecting the condensable fraction.

The output of the condenser was directly connected to GC-TCD injector using an automatic sampling valve for the continuous non-condensable fraction analysis (out of this work). Additionally, a trap filled with quartz wool and magnesium perchlorate was located at the outlet of the quenching system in order to retain non-condensed products and water before the chromatography analysis. The furnace temperature was controlled using an electrical heater and a PID temperature controller. N-type thermocouples were used to measure both temperatures of the furnace and the quartz tube reactor. The desired inert gas flow ( $N_2$ ) was set using a Brooks mass flow controller. The schematically pyrolysis plant is reported in figure S1.

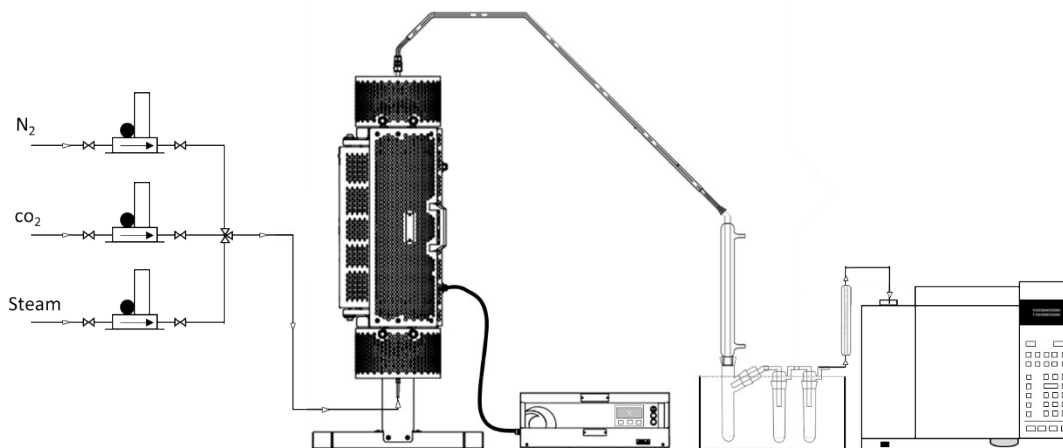


**Figure S1.** The schematically laboratory-scale prototype

## X-ray photoelectron spectroscopy (XPS) analysis of LSW-Biochar

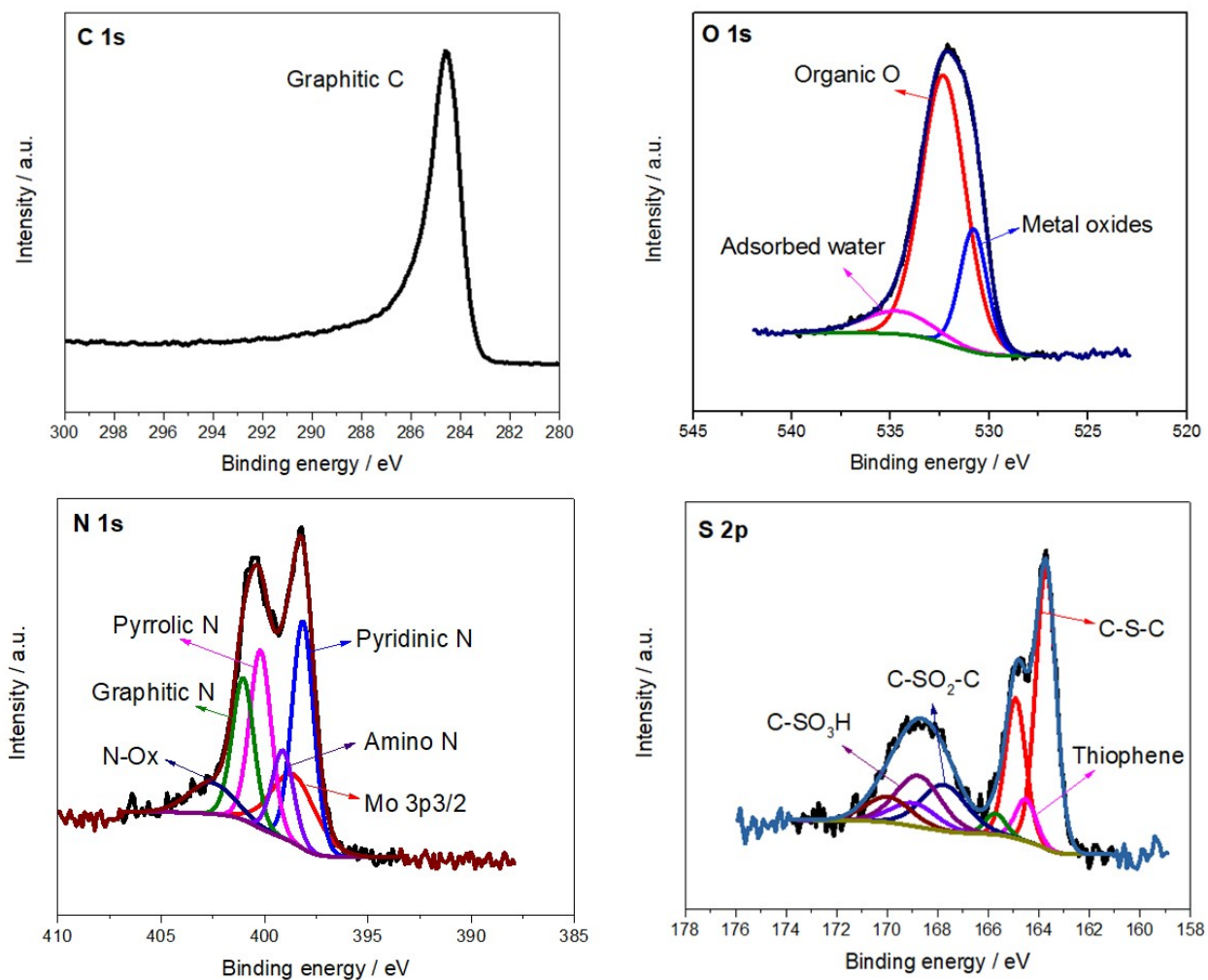


**Figure S2.** XPS spectrum of LSW-Biochar. C 1 s XPS spectrum, O 1s XPS spectrum, and N 1 s XPS spectrum, S 2p XPS spectrum.

## X-ray diffractometer (XRD) analysis of the samples

The interlayer distance between the graphitic layers ( $d_{002}$ ) is calculated by using the Bragg equation:

$$\lambda = 2d_{002} \sin\theta$$

Here,  $\lambda$  is the wavelength of the X-ray beam.

The thickness ( $L_c$ ), and the average width of the graphitic domains ( $L_a$ ) of the carbonized samples are calculated according to the Scherrer's equation:

$$L_c = 0.89\lambda / (\beta_{002} \cos\theta_B) ; L_a = 1.84\lambda / (\beta_{100} \cos\theta_B)$$

where  $\lambda$  is the wavelength of the X-ray beam,  $\beta$  is the peak width at half-maximum intensity (FWHM in radians), and  $\theta_B$  is the Bragg angle (in degrees).

**Table S1:** Parameters calculated from the XRD patterns.

Sample	$L_a$ (nm)	$L_c$ (nm)	$d_{002}$ (nm)	FWHM (002)	FWHM
LSW-Biochar	2.37	0.98	0.359	8.22	7.38
LSW-ACC	2.20	1.01	0.351	7.95	7.96
LSW-ACS	2.08	0.95	0.358	8.43	8.41

## Electrochemical performance of the electrodes

The electrochemical behaviour of LSW-Biochar, LSW-ACS, and LSW-ACC electrodes during the initial ten cycles was evaluated by CV analysis at  $0.05 \text{ mV s}^{-1}$  scan rate. Figure S3 (a-c) shows two reduction peaks at around 1.5 and 0.7 V in the first cycle, which are related to the irreversible reaction of the electrolyte with the surface functionalities of the electrodes, and solid electrolyte interface (SEI) formation, respectively.<sup>1,2</sup> Because of the high level of nitrogen content in the LSW-Biochar and LSW-ACC electrodes, the cathodic peaks at around 0.7 V are not clear, namely the surface of the electrode is relatively resistant to electrolyte degradation.<sup>3</sup> After completing the lithiation process, an anodic peak related to the de-lithiation process is observed at about 0.2 V.<sup>4</sup> Specifically for the LSW-Biochar and the LSW-ACS electrodes, a broad oxidation peak is also observed at about 1 V, and it could be attributed to the faradic capacitance on the surface/edge sites of the biochar product.<sup>5</sup> Furthermore, during the oxidation process in the LSW-Biochar, a narrow peak appeared at around 2.4 V, which could be related to the transformation of  $\text{Li}_x\text{S}$  into polysulfides.<sup>6</sup> Unlike the LSW-Biochar, both LSW-ACS and LSW-ACC electrodes show a considerable overlap in the following cycles demonstrating the high reversibility and the electrochemical stability of the activated electrodes.

Figure S3 (d-f) presents the galvanostatic charge-discharge profiles of LSW-Biochar, LSW-ACS, and LSW-ACC at the current density of  $0.1 \text{ A g}^{-1}$  with respect to the biowaste active material weight. The initial discharge specific capacity of LSW-ACS is  $1520 \text{ mAh g}^{-1}$ , while its first charge specific capacity is  $645 \text{ mAh g}^{-1}$ , which resulted in an initial coulombic efficiency of 42.4%. On the other hand, the initial coulombic efficiency of 38.3% is obtained for LSW-ACC electrode which is attributed to the first discharge specific capacity of  $2063 \text{ mAh g}^{-1}$  and the first charge specific capacity of  $789 \text{ mAh g}^{-1}$ . The non-activated electrode displays the lowest initial specific discharge and charge capacities of 487 and  $194 \text{ mAh g}^{-1}$ , respectively. The remarkably high initial capacity of the activated electrodes compared to the LSW-Biochar is related to their high surface area, high porosity, and to the presence of numerous micro/mesopores defects and vacancies which provide more active sites for storing Li ions.<sup>7</sup>

Figure S3(f) shows a plateau at around 1.6 V during first discharge cycle. This plateau is related to the irreversible reaction of the electrolyte with the surface functional groups of LSW-ACC, confirming the presence of extra elements such as N, O, and S in the  $\text{CO}_2$  activated samples compared to LSW-ACS. A certain amount of these heteroatoms could affect the electron density around N and O atoms, leading to more Li ions holding.<sup>8</sup>

Although both activated electrodes show low initial coulombic efficiencies (a common phenomenon for turbostratic porous carbon structure<sup>9</sup>), at the second cycle it already reaches about 96%, to proceed with the following cycles up to 99%, thus demonstrating the excellent stability of the activated electrodes. The electrolyte degradation of the large specific surface area of LSW-ACS and LSW-ACC electrodes (plateau at around 0.7 V during the first discharge process in galvanostatic charge-discharge profiles), and the irreversible reduction of the functional groups such as dioxygen and oxygenated present in the turbostratic porous biowaste-based electrodes, are the main reasons for the observed initial low efficiency.<sup>8,10</sup>

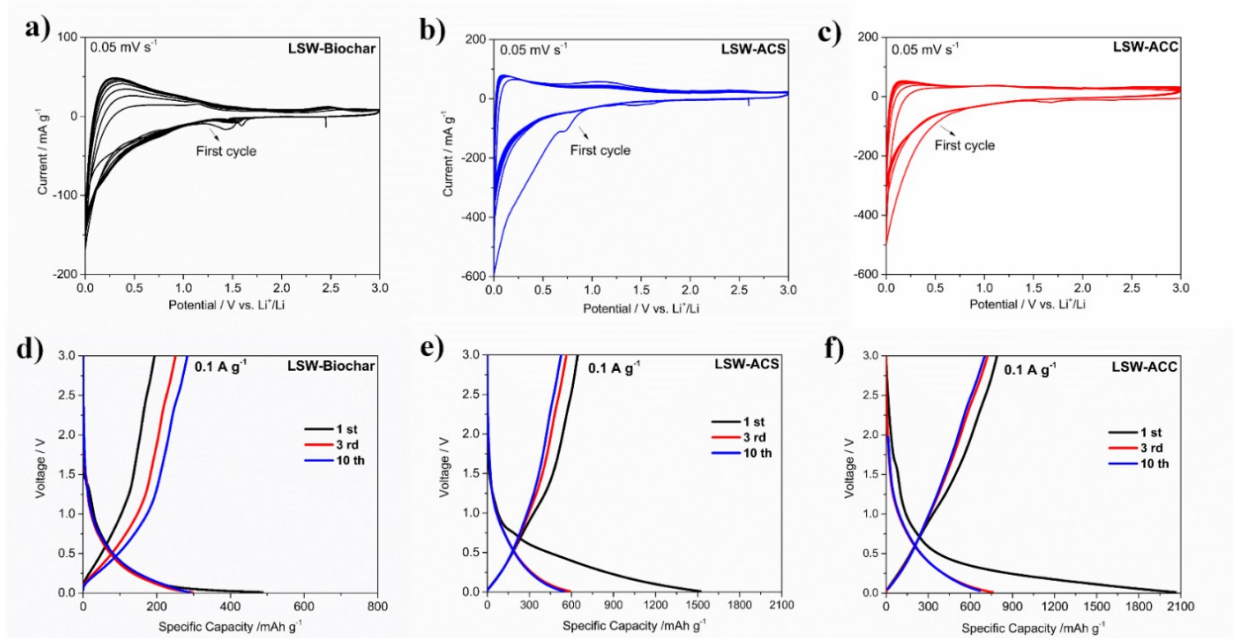


**Figure S3.** (a-c) CV curves of the biowaste electrodes at the scan rate of 0.05 mV s<sup>-1</sup>. (d-f) Galvanostatic charge-discharge profiles performed in lithium-metal half-cell at room temperature within 0.01-3 V. (a, d) LSW-Biochar, (b, e) LSW-ACS, and (c, f) LSW-ACC.

To find the reason for the better electrochemical stability of LSW-ACS electrode than LSW-ACC, and also the reason behind the capacity increase of the activated electrodes after cycling, an AC impedance study was performed after cell assembly and after 500 cycles at 0.5 A g<sup>-1</sup>. The EIS analysis could indeed return the resistance of the charge transfer kinetics through the electrode/electrolyte interface and the SEI film on the activated electrodes, two very important parameters determining the performance of the electrodes in LIBs. The Nyquist plots in Figure S4(a) (fresh state) exhibit a semicircle in the middle frequency region which can be associated to the charge transfer resistance ( $R_{ct}$ ) in the electrolyte/electrode interface, together with a sloped line in the low-frequency region (Warburg impedance). The resistance of the electrolyte ( $R_s$ ) is located before the first semicircle. Observing the Nyquist plots after 500 cycles provides an indication of the resistance of the SEI film that is formed on the surface of the electrodes during cycling. The numerical values of  $R_s$ ,  $R_{sei}$ , and  $R_{ct}$  (Table S2) were calculated by an equivalent circuit model (Figure S4 (b,c)) obtained from Boukamp software. Before cycling,  $R_s$  and  $R_{ct}$  for both activated electrodes are around 10 and 50  $\Omega$ , respectively. However, after 500 cycles,  $R_{ct}$  has decreased down to 8.6  $\Omega$  and 15  $\Omega$  for LSW-ACS and LSW-ACC, respectively. The reduced  $R_{ct}$  value after cycling can be explained through the easy access of the electrolyte to unexposed micro and mesopores sites after several oxidation/reduction reactions. Additionally, the lower  $R_{ct}$  and  $R_{sei}$  values of the LSW-ACS electrode compared to LSW-ACC, suggest an improved electrical conductivity and faster charge transfer kinetics in LSW-ACS, due to a lower presence of heteroatoms and a higher degree of graphitization.

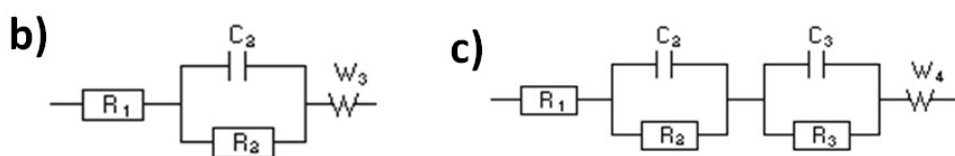
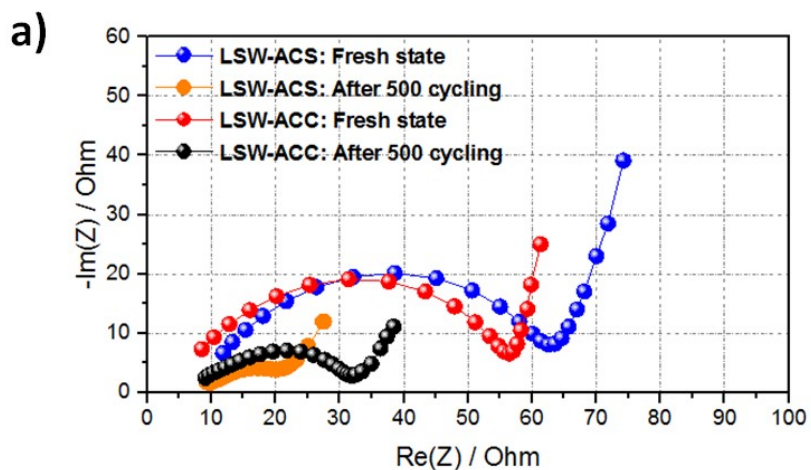


**Figure S4.** a) Nyquist plot of LSW-ACS and LSW-ACC at fresh state, and after 500 cycles at  $0.5 \text{ A g}^{-1}$ . The equivalent circuit is used to fit the experimental impedance spectra for b) fresh state, and c) after 500 cycles.

**Table S2.** The fitting values of  $R_s$ ,  $R_{ct}$ , and  $R_{sei}$  for LSW-ACS and LSW-ACC at fresh state and after 500 charge and discharge cycles run at  $0.5 \text{ A g}^{-1}$ .

State	Resistance ( $\Omega$ )	LSW- ACS	LSW-ACC
Fresh	$R_s$	12.9	9
	$R_{ct}$	49.7	45.9
After 500 cycles	$R_s$	8.9	8.7
	$R_{ct}$	8.6	15
	$R_{sei}$	4	6.9

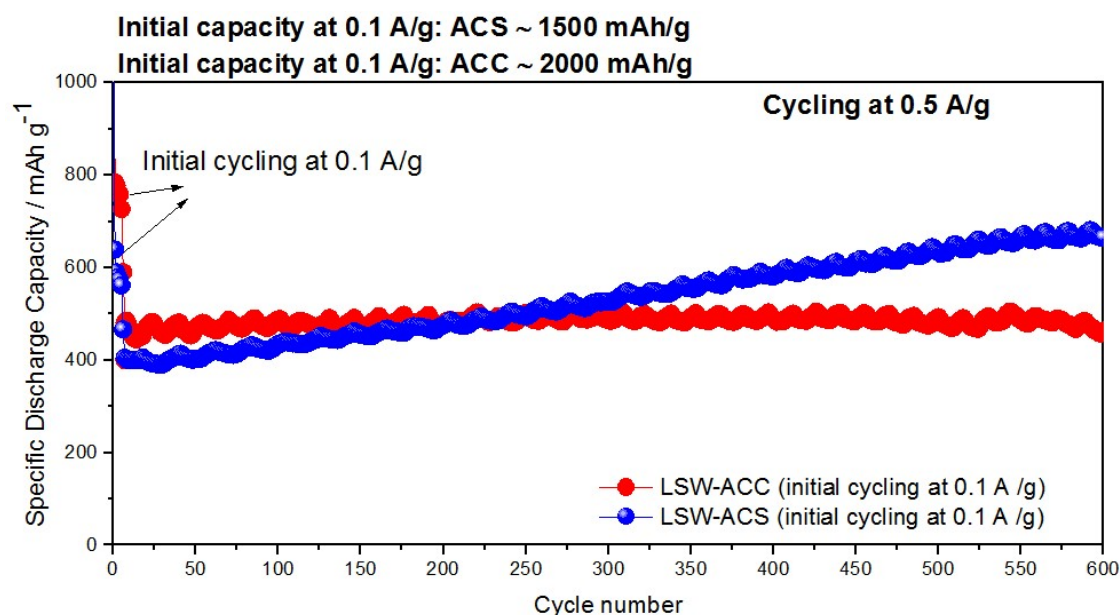


**Figure S5.** Specific discharge capacity for both samples, LSW-ACC and LSW-ACS, at 0.5 A g<sup>-1</sup> after an initial cycling at 0.1 A g<sup>-1</sup>, performed in lithium-metal half cells at room temperature within 0.01-3 V.

**Table S3.** Electrochemical comparison of different LFP cathodes using different carbon-based anodes in LIBs full cells.

Full cell system	Rate (C)	Initial discharge capacity (mA h g <sup>-1</sup> )	Durability/ cycles	Refs.
LFP / A-pBC <sup>1</sup>	0.1	159	77% at 0.1 C / 40 <sup>th</sup>	11
LFP / graphite	0.5	127	65% at 0.5 C / 40 <sup>th</sup>	12
LFP / graphite	0.5	~ 90	~ 89% at 0.5 C / 12 <sup>th</sup>	13
LFP / graphite	0.2	~ 134	24% at 0.2 C / 100 <sup>th</sup>	14
LFP / graphite	0.1	121	52 % at 2 C / 1000 <sup>th</sup>	15
LFP / LSW-ACS	0.1	159	80% at 0.1 C / 50 <sup>th</sup>	<i>This work</i>

<sup>1</sup> Activated pyrolyzed bacterial cellulose

## References

- 1 K. Xu, Y. Li, J. Xiong, X. Ou, W. Su, G. Zhong and C. Yang, *Front. Chem.*, 2018, **6**, 1–10.
- 2 C. Yu, H. Hou, X. Liu, L. Han, Y. Yao, Z. Dai and D. Li, *Front. Mater.*, 2018, **5**, 1–9.
- 3 H. Wan and X. Hu, *Solid State Ionics*, 2019, **341**, 115030.
- 4 V. Mullaivananathan, R. Sathish and N. Kalaiselvi, *Electrochim. Acta*, 2017, **225**, 143–150.
- 5 Z. Nie, Y. Huang, B. Ma, X. Qiu, N. Zhang, X. Xie and Z. Wu, *Sci. Rep.*, 2019, **9**, 1–9.
- 6 H. Shan, X. Li, Y. Cui, D. Xiong, B. Yan, D. Li, A. Lushington and X. Sun, *Electrochim. Acta*, 2016, **205**, 188–197.
- 7 L. Yan, J. Yu, J. Houston, N. Flores and H. Luo, *Green Energy Environ.*, 2017, **2**, 84–99.
- 8 D. Bhattacharjya, H. Y. Park, M. S. Kim, H. S. Choi, S. N. Inamdar and J. S. Yu, *Langmuir*, 2014, **30**, 318–324.
- 9 J. Ou, Y. Zhang, L. Chen, H. Yuan and D. Xiao, *RSC Adv.*, 2014, **4**, 63784–63791.
- 10 J. Xiong, Q. Pan, F. Zheng, X. Xiong, C. Yang, D. Hu and C. Huang, *Front. Chem.*, 2018, **6**, 1–9.
- 11 W. Wang, Y. Sun, B. Liu, S. Wang and M. Cao, *Carbon N. Y.*, 2015, **91**, 56–65.
- 12 T. Wang, X. Yu, M. Fan, Q. Meng, Y. Xiao, Y. X. Yin, H. Li and Y. G. Guo, *Chem. Commun.*, 2019, **56**, 245–248.
- 13 X. Zhang, X. Du, Y. Yin, N. W. Li, W. Fan, R. Cao, W. Xu, C. Zhang and C. Li, *ACS Appl. Mater. Interfaces*, 2018, **10**, 8676–8684.
- 14 J. Ahn, S. Yoon, S. G. Jung, J. H. Yim and K. Y. Cho, *J. Mater. Chem. A*, 2017, **5**, 21214–21222.
- 15 Y. Abe, N. Hori and S. Kumagai, *Energies*, 2019, **12**, 1–14.